Exact self-similarity solution of the Navier–Stokes equations for a porous channel with orthogonally moving walls

Eric C. Dauenhauer
Department of Mechanical Engineering, Stanford University, Stanford, California 94305

Joseph Majdalani[a)]
Mechanical & Industrial Engineering Department, Marquette University, Milwaukee, Wisconsin 53233

(Received 9 November 2001; accepted 21 February 2003; published 2 May 2003)

This article describes a self-similarity solution of the Navier–Stokes equations for a laminar, incompressible, and time-dependent flow that develops within a channel possessing permeable, moving walls. The case considered here pertains to a channel that exhibits either injection or suction across two opposing porous walls while undergoing uniform expansion or contraction. Instances of direct application include the modeling of pulsating diaphragms, sweat cooling or heating, isotope separation, filtration, paper manufacturing, irrigation, and the grain regression during solid propellant combustion. To start, the stream function and the vorticity equation are used in concert to yield a partial differential equation that lends itself to a similarity transformation. Following this similarity transformation, the original problem is reduced to solving a fourth-order differential equation in one similarity variable η that combines both space and time dimensions. Since two of the four auxiliary conditions are of the boundary value type, a numerical solution becomes dependent upon two initial guesses. In order to achieve convergence, the governing equation is first transformed into a function of three variables: The two guesses and η. At the outset, a suitable numerical algorithm is applied by solving the resulting set of twelve first-order ordinary differential equations with two unspecified start-up conditions. In seeking the two unknown initial guesses, the rapidly converging inverse Jacobian method is applied in an iterative fashion. Numerical results are later used to ascertain a deeper understanding of the flow character. The numerical scheme enables us to extend the solution range to physical settings not considered in previous studies. Moreover, the numerical approach broadens the scope to cover both suction and injection cases occurring with simultaneous wall motion. © *2003 American Institute of Physics.* [DOI: 10.1063/1.1567719]

I. INTRODUCTION

Herein we present the details of a procedure that leads to an exact similarity solution of the Navier–Stokes equations in semi-infinite rectangular channels with porous and uniformly expanding or contracting walls. The solution to be developed is aimed at characterizing the flow field established in such a physical setting. One of the primary objectives of this study is to extend our current knowledge of laminar flows involving channels with porous walls by encompassing moving boundaries.

Laminar flow studies in permeable walls have received considerable attention in the past due to their relevance in a number of engineering applications. These include binary gas diffusion, filtration, ablation cooling, surface sublimation, grain regression (as in the case of combustion in rocket motors), and the modeling of air circulation in the respiratory system.

The earliest studies of steady flows across permeable and stationary walls can be traced back to Berman.[1] Therein, Berman investigated the laminar, two-dimensional flow of a viscous incompressible fluid driven by uniform injection (or suction) in a rectangular channel with porous walls. In his study, Berman[1] assumed that the transverse velocity component was independent of the streamwise coordinate. He thus reduced the Navier–Stokes equations to a single, nonlinear, fourth-order, ordinary differential equation (ODE) with four boundary conditions and a cross-flow Reynolds number R. The latter was based on the normal injection speed v_w and channel half-spacing $a(t)$. For small R, he employed a regular perturbation scheme to derive an asymptotic formulation. Numerous studies of channel flows with permeable walls followed. Among these are the works of Terrill,[2] who extended Berman's small R case, and Proudman,[3] who investigated the large R case using an integral approach. Morduchow[4] later applied the method of averages for his solution over the full injection range. White, Barfield, and Goglia,[5] on the other hand, provided a convergent power series solution for arbitrary R. This was followed by Sellars[6] who investigated the large suction case and, subsequently, by Taylor[7] and Yuan[8] who provided asymptotic solutions for the infinite and large injection cases, respectively. Finally, higher-order corrections to Yuan's work were provided by Terrill.[9]

For asymmetrical flows caused by different wall velocities, Terrill and Shrestha[10] constructed a generalized pertur-

a)Author to whom correspondence should be addressed. Telephone: (414) 288-6877; fax: (414) 288-7082; electronic mail: maji@mu.edu

 © 2003 American Institute of Physics

bation series for small R. For large injection, Shrestha and Terrill[11] extended Proudman's one-term expression using matched asymptotic expansions. In the same vein, Cox[12] considered the practical case of an impermeable wall opposing a transpiring wall.

The treatment of moving boundaries can be traced back to Brady and Acrivos[13] whose endeavor has led to an exact solution of the Navier–Stokes equations for a flow driven by an axially accelerating surface velocity and symmetric boundary conditions. Their work was motivated by the need to study long slender droplets trapped in extensional flows. This effort was made more general by Watson *et al.*[14] who allowed the accelerating walls to be porous. Watson *et al.*[15] also examined the case of asymmetrically accelerating walls. Other geometrical settings have been considered[16] and the role of spatial[17] and hydrodynamic[18] flow instabilities have received due attention, especially in the recent studies by Casalis, Avalon, and Pineau,[19] and Griffond and Casalis.[20,21]

In validating the similarity solutions recounted above, investigators have often relied on numerical simulations. Extensive experimental verifications have also been accomplished.[19–25] In fact, numerous laboratory experiments on porous channel flows have been conducted by Taylor,[7] Wageman, and Guevara,[26] Varapaev and Yagodkin,[27] Raithby and Knudsen,[28] and Sviridenkov and Yagodkin.[29] In recent studies of aeroacoustic instabilities in porous enclosures, Casalis and colleagues[19–21] have reproduced the injection driven flow in a controlled and windowed environment known as the *Veine d'Études de la Couche Limite Acoustique* (VECLA) facility. Theirs consisted of a long rectangular channel with one hard wall facing a porous wall across which air injection could be imposed. The main focus of their work was the addition of time-dependent acoustic waves that could lead to highly vortical and turbulent fields.

The addition of time-dependent motion in a long rectangular channel with porous walls was first achieved experimentally by Ma, Van Moorhem and Shorthill,[24,25] and Barron, Van Moorhem, and Majdalani.[22] In fact, both used the sublimation process of carbon dioxide to simulate the injection process at the walls. As a result, the walls of their channel expanded during the sublimation process. Other physical settings that can be modeled with expanding permeable walls include the regression of the burning surface in solid rocket motors and the synchronous pulsation of porous diaphragms.

In simulating the laminar flow field in an idealized solid rocket motor, Goto and Uchida[30] have analyzed the laminar incompressible flow in a semi-infinite porous pipe whose radius varies with time. The present treatment extends their analysis to expanding or contracting channels with porous walls experiencing wall injection and suction over a broad range of operating conditions. It also offers basic insights into the essential flow features and discusses the existence of boundary layers and nonunique solutions that require further analysis.

The current investigation starts in Sec. II by introducing the geometry, governing equations, and boundary conditions. Through the introduction of the stream function, the governing equations are reduced to a single, fourth-order, partial differential equation (PDE). Next, a stream function solution is posited in Sec. III and similarity solutions in space and time are developed to convert the PDE to an ODE. This fourth-order ODE is then solved numerically using a shooting method described in the Appendix. Section IV serves to characterize the flow field by transforming the numerical results to physically significant relationships. The resulting flow phenomena for our particular problem are discussed in Sec. V and concluding remarks are compiled in Sec. VI.

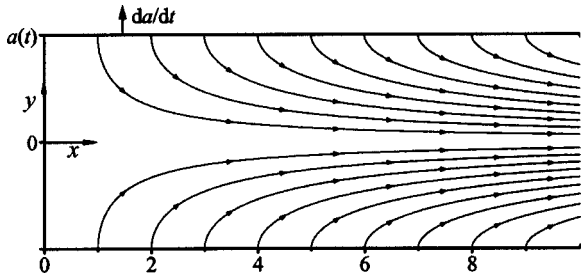

FIG. 1. Coordinate system and bulk fluid motion.

II. FORMULATION

To begin, we consider an elongated rectangular channel exhibiting a sufficiently large aspect ratio of width w to height a $(w/a>4)$. Despite the channel's finite body length, it is commonplace to assume semi-infinite length in order to neglect the influence of the opening at the end.[31] The head-end, however, is closed by a solid, impermeable membrane that is allowed to stretch with channel expansions or contractions. As shown in Fig. 1, the streamwise flow is zero at the closed end $(x=0)$. With x indicating the streamwise direction and y the normal direction, the corresponding streamwise and transverse velocity components are defined as u and v, respectively. In this two-dimensional notation, the equations governing the unsteady flow of an incompressible fluid are the differential expressions for mass and momentum conservation. These are given by

$$\frac{\partial u}{\partial x}+\frac{\partial v}{\partial y}=0, \tag{1}$$

$$\frac{\partial u}{\partial t}+u\frac{\partial u}{\partial x}+v\frac{\partial u}{\partial y}=-\frac{1}{\rho}\frac{\partial p}{\partial x}+\nu\left(\frac{\partial^2 u}{\partial x^2}+\frac{\partial^2 u}{\partial y^2}\right), \tag{2}$$

$$\frac{\partial v}{\partial t}+u\frac{\partial v}{\partial x}+v\frac{\partial v}{\partial y}=-\frac{1}{\rho}\frac{\partial p}{\partial y}+\nu\left(\frac{\partial^2 v}{\partial x^2}+\frac{\partial^2 v}{\partial y^2}\right), \tag{3}$$

where ρ, p, ν, and t are the dimensional density, pressure, kinematic viscosity, and time. The channel walls of interest regress or contract only in the transverse direction. Hence, their separation $a(t)$ is only a function of time. Under the porous wall stipulation, the fluid is injected or aspirated uniformly and orthogonally through the channel walls at an absolute velocity v_w, thereby establishing a symmetric flow field about the midsection plane (at $y=0$). It should be noted that possible asymmetric bifurcations that could suddenly emerge would not be captured in the present approach due to the artificially imposed symmetry about the midsection plane. According to our adopted nomenclature, v_w will be positive for injection and negative for suction. Defining the

problem in a half-domain, the boundary conditions necessary for solving the continuity and momentum equations are, as usual:

$$u=0 \quad v=-v_w; \quad y=a(t), \tag{4}$$

$$\frac{\partial u}{\partial y}=0 \quad v=0; \quad y=0, \tag{5}$$

$$u=0 \quad v=0; \quad x=0. \tag{6}$$

The end wall, as alluded to in Eq. (6), is assumed to be the center of the classic squeeze film problem, thereby establishing symmetry at the origin. It is this symmetry, and the no-slip condition, that cause both u and v to vanish at $x=0$. The assumption that the absolute inflow velocity v_w is independent of position implies that the fluid injection speed v_b relative to the wall must be spatially uniform by virtue of the fundamental relation $v_w \equiv v_b - \dot{a}$. Seemingly, a contracting wall (one with negative $\dot{a}$) has the same effect on the fluid as that of injection, viz. it can increase the absolute injection velocity (or reduce the suction velocity) at the wall. In the hypothetical case of rigid walls, the relative fluid permeation speed with respect to the walls will be zero and the absolute injection velocity will be equal to $-\dot{a}$. The converse is true for expansion since regression has the same effect as suction at the walls. While v_w and $\dot{a}$ may be independent in nonreactive experiments, they are related in active propellants by the solid-to-gas density ratio. This can be explained by referring to the mass conservation equation at the propellant-gas interface. If we let ρ_s be the propellant density, then conservation of mass at the burning surface requires that $\rho A_b v_b = \rho_s A_b \dot{a}$, where A_b represents the burning area. Thus, the gas velocity with respect to the wall can be deduced to be

$$v_b = (\rho_s/\rho)\dot{a} \equiv r_\rho \dot{a}, \tag{7}$$

where r_ρ is the solid-to-gas density ratio. From Eq. (7) the absolute velocity is observed to be a function of the deformation speed $\dot{a}$ via $v_w = (r_\rho - 1)\dot{a} = A\dot{a}$, where $A = r_\rho - 1$ is the injection coefficient.[30] Since $A = v_w/\dot{a}$, it can be estimated in rocket motors to be $A \sim r_\rho \sim 100$ for a typical $\rho_s \sim 2000\ \mathrm{kgm}^{-3}$ and $\rho \sim 20\ \mathrm{kgm}^{-3}$. Ultimately, the injection coefficient A may be viewed as a measure of the porosity of the wall and can be utilized as a control parameter in the final solution.

By applying mass conservation to a volume ϑ of fluid extending from the end wall ($x=0$) to an arbitrary location x, the flow velocity $u_m(x,t)$ spatially averaged over the cross section can be found to be proportional to x. To that end, the mean flow velocity u_m must be determined from

$$u_m(x,t) = \left(\int_{A_c} \mathbf{u}(x,y,t) \cdot d\mathbf{A} \right) \Big/ A_c \tag{8}$$

where $A_c = 2aw$ is the surface area of the cross section. However, since $A_b = 2xw$ is the channel's porous area, conservation of mass in integral form requires that

$$-\frac{\partial}{\partial t}\int_\vartheta \rho d\vartheta + \rho A_b v_b - \int_{A_c} \rho \mathbf{u} \cdot d\mathbf{A} = 0, \tag{9}$$

where $d\vartheta = d(2axw)$. By virtue of Eq. (8), Eq. (9) becomes

$$-\rho x \frac{\partial A_c}{\partial t} + \rho A_b v_b - \rho A_c u_m = 0, \tag{10}$$

therefore,

$$u_m = \frac{A_b}{A_c} v_b - \frac{x}{A_c}\frac{\partial A_c}{\partial t} = \frac{x}{a}(v_b - \dot{a}) = \frac{x}{a} v_w. \tag{11}$$

It can be inferred from Eq. (11) that the mean velocity u_m varies linearly with x. The choice of a self-similarity transformation that can result in such a variation is, therefore, desirable. Such a transformation will be presented next. But first, we find it convenient to introduce the stream function and, thereby, allow the replacement of the two velocity components with a single function satisfying

$$u = \frac{\partial \psi}{\partial y} \quad \text{and} \quad v = -\frac{\partial \psi}{\partial x}. \tag{12}$$

From this definition of the stream function, the continuity equation becomes self-satisfied and, hence, no longer useful in determining ψ. A new variable can now be removed at the expense of introducing another. In fact, taking the curl of the momentum equation produces the vorticity transport equation for the given geometry. One gets

$$\frac{\partial \zeta}{\partial t} + u\frac{\partial \zeta}{\partial x} + v\frac{\partial \zeta}{\partial y} = \nu\left(\frac{\partial^2 \zeta}{\partial x^2} + \frac{\partial^2 \zeta}{\partial y^2}\right), \tag{13}$$

where

$$\zeta = \frac{\partial v}{\partial x} - \frac{\partial u}{\partial y} = -\nabla^2 \psi. \tag{14}$$

Finally, inserting Eqs. (12) and (14) back into Eq. (13), one can write

$$\frac{\partial}{\partial t}\nabla^2\psi + \frac{\partial \psi}{\partial y}\frac{\partial}{\partial x}\nabla^2\psi - \frac{\partial \psi}{\partial x}\frac{\partial}{\partial y}\nabla^2\psi = \nu\nabla^2\nabla^2\psi. \tag{15}$$

III. MATHEMATICAL PROCEDURE

A. Similarity solution in space

A Hiemenz type similarity solution with respect to x can be developed due to mass conservation and the fact that the channel height remains constant in the streamwise direction.[32] In view of the boundary conditions given by Eqs. (4) and (5), we find a stream function solution of the form

$$\psi = (\nu x/a) F(\eta, t), \tag{16}$$

where $\eta = y/a$ and $F(\eta,t)$ is independent of the streamwise coordinate. With this realization, the streamwise and transverse velocities can be written in their final form, namely, as

$$u = \nu x a^{-2} F_\eta \quad \text{and} \quad v = -\nu a^{-1} F(\eta, t), \tag{17}$$

where $F_\eta = \partial F/\partial \eta$. Upon substitution of ψ into Eq. (15), one obtains a differential equation for the main characteristic function F. This is

$$[F_{\eta\eta\eta} + FF_{\eta\eta} + F_\eta(2\alpha - F_\eta) + \alpha\eta F_{\eta\eta} - (a^2/\nu)F_{\eta t}]_\eta = 0, \tag{18}$$

where α is the wall expansion ratio defined as

$$\alpha(t)=\dot{a}a/\nu. \tag{19}$$

Note that allowing $p_{xy}=0$ in Eq. (2) will also lend itself as a method of arriving at Eq. (18). The boundary conditions given by Eqs. (4) and (5) can now be updated to account for the normalization. One finds

$$\eta=0: \quad F=0, \quad F_{\eta\eta}=0, \quad \eta=1: \quad F=R, \quad F_{\eta}=0, \tag{20}$$

where $R=v_w a/\nu=A\alpha$.

B. Similarity solution in space and time

A similarity solution with respect to space and time can now be developed. If our function F is made dependent on η and $\alpha(t)$ instead of (η,t), we can then obtain $F_{\eta t}=0$ by setting α to be constant or quasi-constant in time. In that event, the value of the expansion ratio α can be specified by its initial value

$$\alpha=\dot{a}a/\nu=\dot{a}_0 a_0/\nu, \tag{21}$$

where a_0 and $\dot{a}_0=\mathrm{d}a_0/\mathrm{d}t$ denote the initial channel height and channel expansion rate, respectively. By integrating Eq. (21) with respect to time, a similar solution for the temporal channel height evolution can be obtained. This is given by

$$a(t)/a_0=(1+2\nu\alpha t a_0^{-2})^{1/2}. \tag{22}$$

For a physical setting in which the injection coefficient A is constant (e.g., burning propellant), an expression for the time-dependent injection velocity evolution can be deduced to yield

$$\dot{a}/\dot{a}_0=v_w(t)/v_w(0)=(1+2\nu\alpha t a_0^{-2})^{-1/2}. \tag{23}$$

Under the foregoing self-similarity conditions, an ODE for the principal function F can be derived by direct integration of Eq. (18). One obtains

$$F'''+FF''+F'(2\alpha-F')+\alpha\eta F''=K, \tag{24}$$

where a prime replaces $\mathrm{d}/\mathrm{d}\eta$ and K is the constant of integration. The necessary boundary conditions translate into

$$\eta=0: \ F=F''=0, \quad \eta=1: \ F=R, \ F'=0. \tag{25}$$

From the exercise described above, a possible solution may be found through similarity arguments and the assertion that $\alpha=$ constant. Although outside the scope of the present treatment, it should be noted that all of the admissible similarity solutions may be found by using Lie group theory for which many references are available. Moreover, in view of the nonlinearity of Eq. (24), nonunique solutions are likely to exist. Although solution multiplicity is not considered by Goto and Uchida,[30] the analogous problems studied by Berman[1] and Terrill[33] in which wall motion is suppressed has exhibited multiple solutions while increasing the cross-flow Reynolds number. Some of these solutions have been shown to become unstable to time-dependent perturbations, thus leading to pitchfork bifurcations, stable asymmetric steady solutions, Hopf bifurcations, stable time-periodic solutions, stable quasi-periodic solutions, phase locking, and chaos.[34] Further effort to investigate the stability of the current solution in porous channels and pipes with expanding walls is clearly needed following the lines described by Zaturska, Drazin, and Banks.[34] In the analogous problem with no wall motion, it is interesting to note that the injection solution was found to be unique and stable for the entire range of cross-flow Reynolds number, $R\in[0,\infty)$. A similar character was observed in computational results. For the suction driven channel flow with no wall motion, Zaturska, Drazin, and Banks,[34] have shown that one symmetric solution exists for $R\in[-12.165,0]$ and three symmetric solutions emerge when $R\in(-\infty,-12.165]$. In much the same manner, the search for multiple solutions in the present analysis will be influenced by both R and α, thus requiring a separate mathematical treatment. Since the porous channel and tube with stationary walls were covered in a series of successive studies,[33–42] the current configuration is likely to motivate further exploration—especially at sufficiently large $|R|$.

IV. FLOW FIELD CHARACTERIZATION

A. Nondimensional variables

Once we obtain a numerical solution for F, the dimensionless stream function and velocity components become available. The numerical solution is based on a rapidly converging shooting technique described in the Appendix. The scheme we use enables us to extend the results over a broader range of operating parameters than used previously.[30] Our approach requires guesswork until a convergent solution is reached. In the process, several guesses are attempted each time to ensure a uniquely convergent solution. Nonetheless, the effort to determine the proper initial guesses is found to increase rapidly with successive increases in $|R|$, especially in the suction case. Hence, it is likely that not all possible solutions at large $|R|$ have been captured. Recently, a similar set of equations arising in the analogous time-dependent Berman problem has been shown to require special numerical treatment by King and Cox.[37] Accordingly, the numerical solution of the corresponding equation becomes infeasible below $R=-90.9$.

The stream function can be normalized by its value at the wall $(\eta=1)$ in view of Eq. (25); letting $\psi(1)=\nu x F(1)/a=\nu x R/a$, we then write

$$\psi^*=\psi/\psi(1)=F/R. \tag{26}$$

In view of Eqs. (17) and (11), the streamwise velocity can be normalized by the mean streamwise velocity such that

$$u^*=u/u_m=F'/R. \tag{27}$$

One may note that the result is independent of the streamwise position. Profiles of u^* can then be displayed for small, moderate, and large injection and suction in Figs. 2 and 3, respectively.

Finally, since the velocity at the wall may be expressed as $v(1)=-v_w=-\nu R/a$, the normal velocity may be referenced to the value at the wall such that

$$v^*=v/v(1)=\psi/\psi(1)=F/R. \tag{28}$$

The normalized stream function and normal velocity components are, therefore, identical and can be illustrated in Fig. 4 for both small-to-moderate injection and suction.

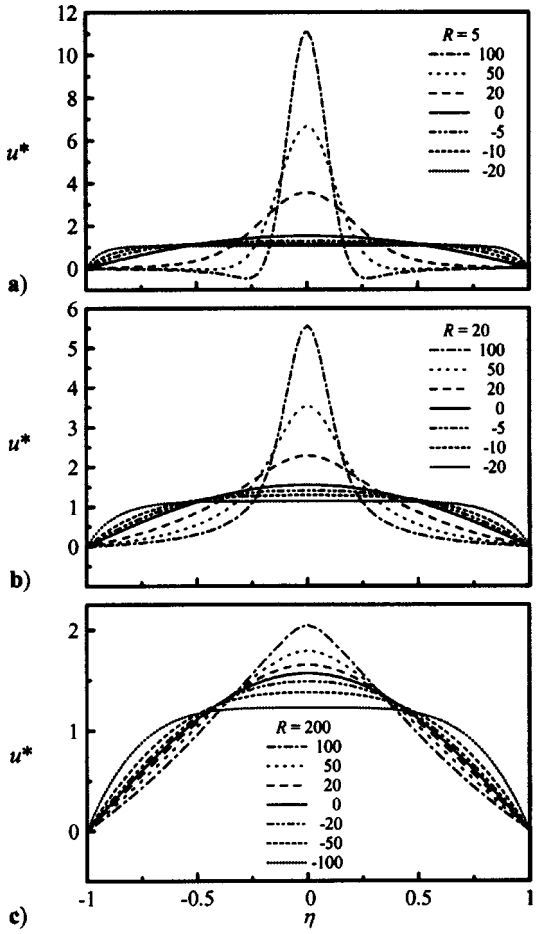

FIG. 2. Streamwise velocity profiles shown over a range of wall expansion (or contraction) ratios and an injection Reynolds number of (a) 5, (b) 20, and (c) 200.

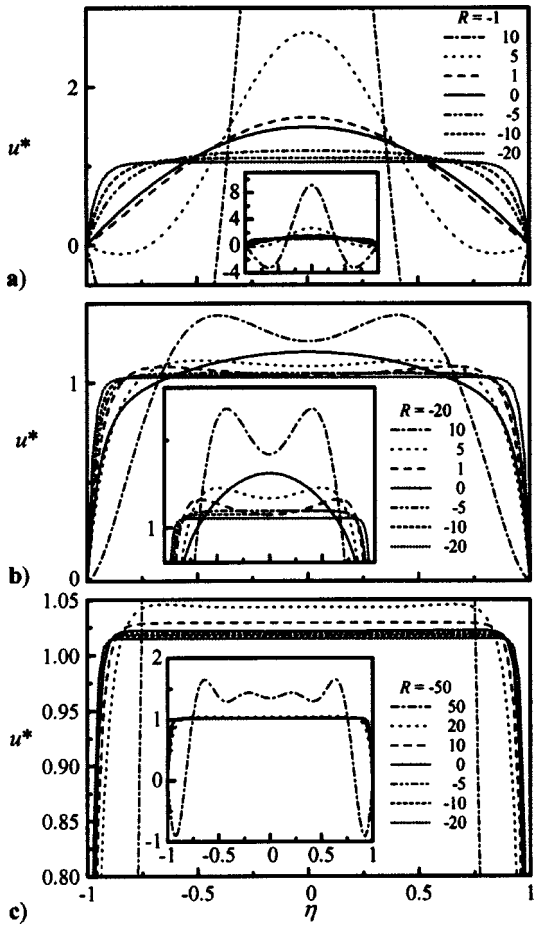

FIG. 3. Streamwise velocity profiles shown over a range of wall expansion ratios and a suction Reynolds number of (a) -1, (b) -20, and (c) -50.

B. Pressure and shear

To complete our flow field analysis, the resulting pressure gradients and shear stress distributions are considered as well. An expression for the normal pressure gradient can be developed by substituting the velocity components of Eq. (17) into Eq. (3) with F acting as a function of η only. The result is

$$p_{\eta} = -\nu^2 \rho a^{-2}[F_{\eta\eta} + FF_{\eta} + \alpha(F + \eta F_{\eta})]. \tag{29}$$

The normal pressure distribution is revealed by manipulating Eq. (29) before integrating and applying the boundary conditions of Eq. (25). Proceeding by writing

$$\int_{p(x,0)}^{p(x,\eta)} \mathrm{d}p$$

$$= -\int_0^{\eta} \rho \nu^2 a^{-2}[F_{\eta\eta} + FF_{\eta} + \alpha(F + \eta F_{\eta})]\mathrm{d}\eta, \tag{30}$$

the pressure distribution in the normal direction can be nondimensionalized and written as

$$p_{\mathrm{n}}^{*} = [p(x,\eta) - p(x,0)]a^2/(\rho\nu^2)$$

$$= F_{\eta}(0) - \left(\alpha\eta F + \frac{1}{2}F^2 + F_{\eta}\right). \tag{31}$$

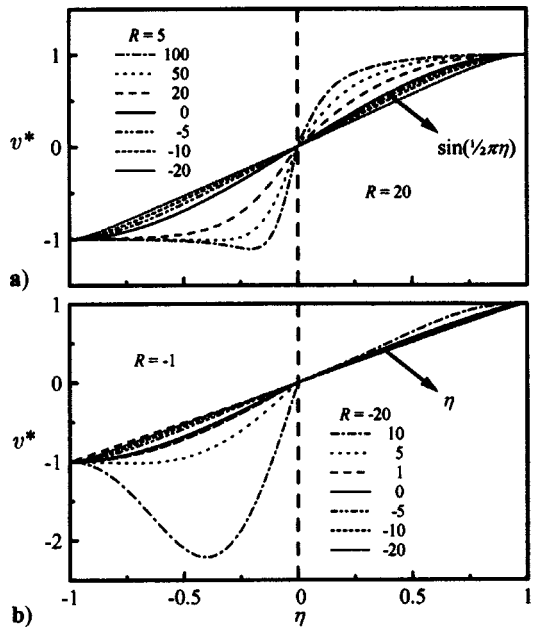

FIG. 4. Normal velocity profiles shown over a range of expansion ratios and cross-flow Reynolds numbers corresponding to (a) injection and (b) suction.

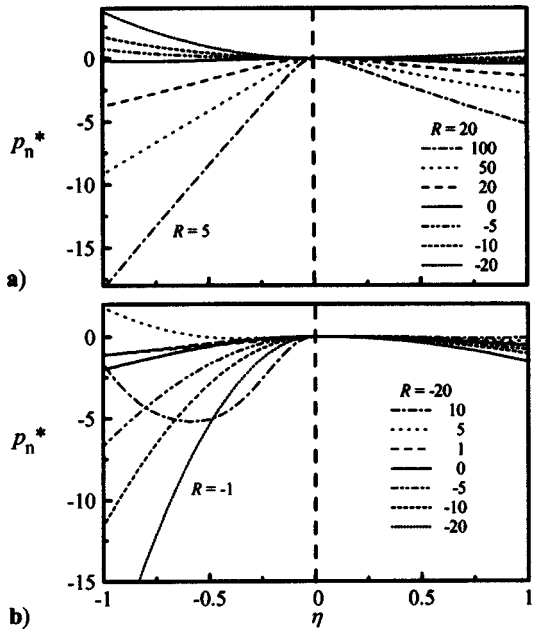

FIG. 5. Normal pressure drop shown over a range of expansion ratios and cross-flow Reynolds numbers corresponding to (a) injection and (b) suction.

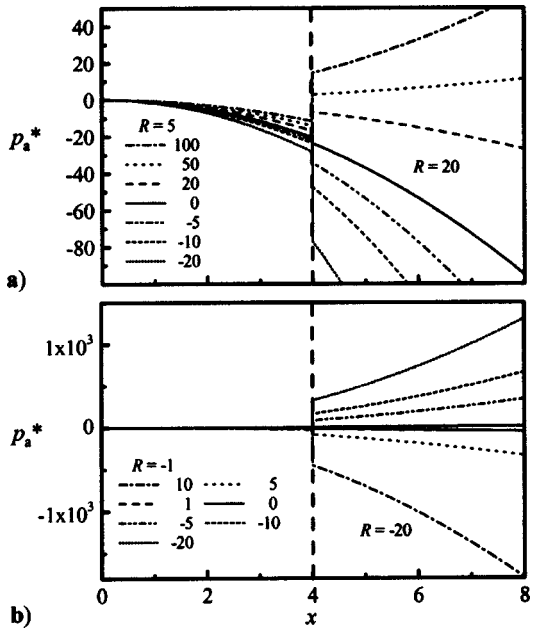

FIG. 6. Streamwise pressure drop over a range of α and R corresponding to (a) injection and (b) suction.

The normal pressure drop p_n^* can now be plotted in Fig. 5 over a range of α and R.

Since F behaves as a function of η only and $F_{\eta t}=0$ in the streamwise direction, substitution of the velocity components from Eq. (17) into the streamwise momentum of Eq. (2) yields the streamwise pressure gradient

$$\frac{\partial p}{\partial x}=\rho\nu^2 a^{-4}x[F'''+FF''+F'(2\alpha-F')+\alpha yF'']. \quad (32)$$

In light of Eq. (24), Eq. (32) be simplified to

$$\frac{\partial p}{\partial x}=\rho\nu^2 x a^{-4}K. \quad (33)$$

This expression can be readily integrated and nondimensionalized to obtain the streamwise pressure distribution at any streamwise position

$$p_a^*=\frac{p(x,\eta)-p(0,\eta)}{(\rho\nu^2/a^2)}\frac{a^2}{a_0^2}=\frac{1}{2}Ka_0^{-2}x^2. \quad (34)$$

The streamwise pressure drop p_a^* can be illustrated in Fig. 6 by plotting it over a range of α and R.

Finally, the shear stress due to flow past the porous surface can be determined from Newton's law for viscosity, namely

$$\tau=\mu\left(\frac{\partial u}{\partial y}+\frac{\partial v}{\partial x}\right). \quad (35)$$

Thus, by substituting the velocity components from Eq. (17) into the shear stress equation, one may nondimensionalize after expressing the results at the wall. One finds

$$\tau^*=\frac{\tau_w}{(\rho\nu^2/a_0^2)}\frac{a^3}{a_0^3}=(x/a_0)F''(1), \quad (36)$$

where τ^* represents the dimensionless stress at the wall. The shear stress can be described in Fig. 7 by plotting it over a range of α and R.

V. RESULTS

In an effort to develop a better understanding of the effects of viscosity and wall deformation on the flow character, the main flow attributes are described over different ranges of the control parameters R and α. This additional insight into the physics of the problem may be achieved through a detailed interpretation of the streamwise and normal veloci-

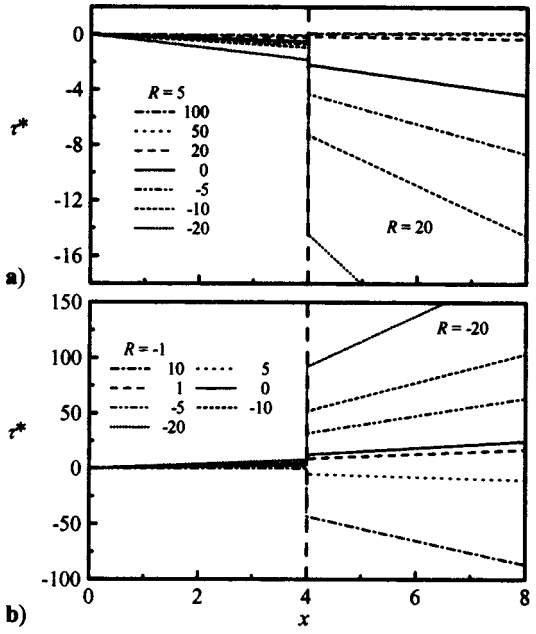

FIG. 7. Same as previous for wall shear stress.

ties, streamwise and normal pressure distributions, shear stress at the wall, and the streamline behavior.

A. Streamwise velocity

Figure 2 illustrates the behavior of the streamwise velocity profiles for low, moderate, and high injection Reynolds numbers taken over a range of wall expansion–contraction scenarios. An initial glance indicates the greater sensitivity to wall regression at the low injection case of $R=5$ [Fig. 2(a)]. This phenomenon manifests itself in the form of flow reversal that is most clearly depicted in the $R=5$, $\alpha=100$ case. Therein, the rate of expansion is very large compared to the rate of mass addition at the boundaries. The rapid volumetric expansion of the walls creates suction regions near the closed head-end where a mass deficiency is suddenly formed. The incompressible fluid is thus forced upstream in the head-end direction in order to occupy the space accompanying the expansion process. The same fluid has to later turn and head downstream towards the open end. It should be noted that flow reversal seems to occur, in all cases, when the relative injection ratio, $|\alpha/R|$, exceeds the value of 10. As such, the $R=5$, $\alpha=50$ case may be seen, in Fig. 2(a), to delimit the borderline beyond which flow reverses.

If the injection is large enough, however, flow reversal can be suppressed, as Figs. 2(b) and 2(c) would indicate. Under such circumstances, the fluid that enters the channel can rapidly fill the gap created by the moving walls in a manner to mitigate flow reversal. Note, in particular, the $R=20$, $\alpha=100$ case in Fig. 2(b) where the flow is at the verge of flow reversal. Such a situation can arise when the moderate injection Reynolds number is able to compensate for the rapid wall expansion rate. The absence of flow reversal is also consistent with the criterion that we have set earlier since the relative expansion to injection ratio in the case-at-hand happens to be $|\alpha/R|=5<10$. For added clarity, the injection-driven streamlines are furnished in Figs. 8(a)–8(c).

As an aside, it may be interesting to note the special case of stationary walls at $\alpha=0$, $R=0$ where the centerline-to-mean velocity ratio, $u^*(0)$, is equal to 3/2. This value matches the centerline-to-mean velocity ratio in the fully developed Hagen–Poiseuille flow whose profile is parabolic. Scenarios involving injection $(R>0)$ increase $u^*(0)$ above 3/2 due to the addition of mass at the walls while cases with suction $(R<0)$ will exhibit a reduction from this value.

Figure 3 presents the streamwise velocity profiles that occur for low, moderate, and high suction Reynolds numbers. Here too, a flow reversal mechanism that is similar to that described for injection can take place. In fact, flow reversal can be seen in Figs. 3(a) and 3(c), for the $R=-1$, $\alpha=5,10$, and $R=-50$, $\alpha=50$ cases. In all cases, the relative suction ratio satisfies $|\alpha/R|\geqslant 1$. Moreover, it appears that flow reversal begins when the expansion to suction ratio exceeds 1. Since the volumetric expansion rate is appreciable in comparison to the fluid withdrawal rate, the inception of suction regions near the head-end causes the fluid to move farther upstream to occupy the rapidly created space near the closed end. The same fluid that has moved upstream has to later swerve and head downstream towards the suction sites

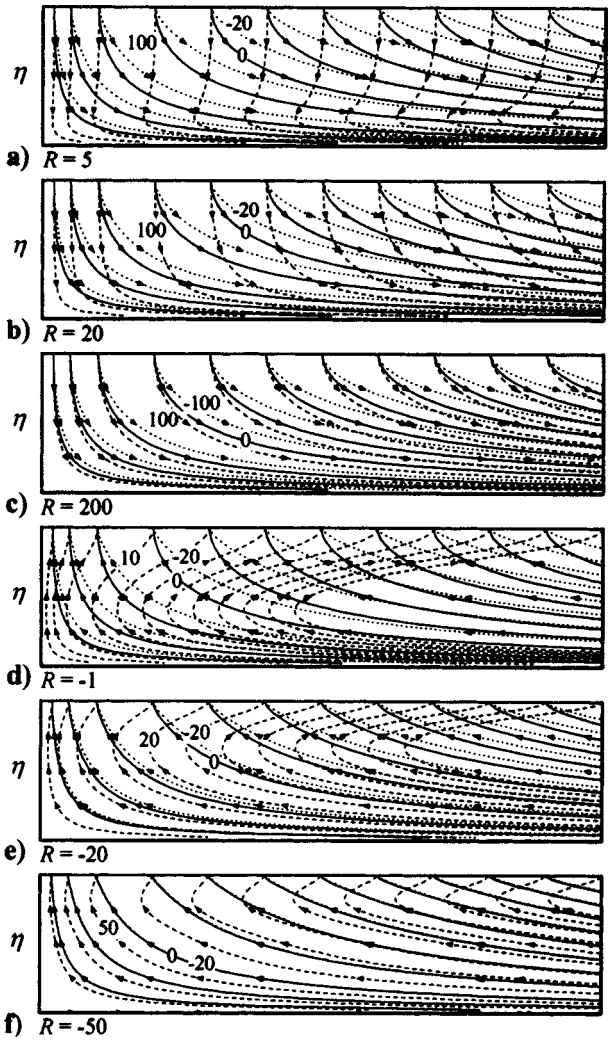

FIG. 8. Flow streamlines shown over a range of expansion ratios and cross-flow Reynolds numbers. While the motionless case ($\alpha=0$) is represented by solid lines, wall expansions and contractions ($\alpha>0,\alpha<0$) are denoted by dotted and dashed lines, respectively.

along the porous surface. This behavior can be clearly seen in Figs. 8(d)–8(f) where flow streamlines are illustrated.

For increasing suction, one observes in Figs. 3(b) and 3(c) that the velocity profiles gradually become more flat while asymptoting to a spatially uniform value. The flattening in the profile is, of course, indicative of thinning boundary layers and is consistent with classic laminar flow theory. In this problem, sufficiently large suction can dominate over wall expansion and attract the shear layers closer to the walls. In similar suction-driven flows with stationary walls, the boundary layer forming above the wall was shown to become thinner with successive increases in $|R|$.[34,35]

Increasing wall contraction, on the other hand, causes the profile to level-off more rapidly such that $u^*(0)\to 1$ at lower values of suction. This phenomenon is clearly seen in Figs. 3(a)–3(c) for $\alpha<0$. As such, one may conceive of an effective suction Reynolds number, $R_s=-(R+\alpha)$, that combines the convective effects of the aspiration with those of the wall motion. By running multiple tests, we find that as R_s increases beyond 20, the flow approaches the inviscid

flow solution that exists for infinitely large suction. The solution dependence on an effective Reynolds number R_s can be tacitly confirmed by an asymptotic treatment which can be carried out straightforwardly for the large suction case.

B. Normal velocity

The behavior of the normal velocity is illustrated in Fig. 4 wherein four values of the cross-flow Reynolds number are presented on two sets of axes for purposes of compactness and ease of comparison. Two interesting phenomena can be observed from these profiles. The first corresponds to the existence of a point on the interval $-1<\eta<0$ where the normal velocity exceeds its (absolute) value at the wall. This is, again, most noticeable in the low injection and suction cases [left halves of Figs. 4(a) and 4(b)] where flow reversal is observed. This occurs during rapid wall expansions and contractions leading to $|\alpha/R|$ in excess of 10 for injection [Fig. 4(a)], and 1 for suction [Fig. 4(b)]. For the scenario of low flow injection into a rapidly expanding channel, as seen in Fig. 4(a), the point of maximum normal velocity moves away from the wall in order to satisfy mass conservation. As the injected flow turns towards the head-end, it collides with the incoming stream along the upstream sections of the porous surface. This causes the normal velocity to overshoot above its value at the wall in order to compensate for a larger influx per unit area. The transverse velocity overshoot seen in Fig. 4 can be attributed to the presence of flow reversal and collision regions. These so-called collision regions have been observed in other studies by Brady[43] and Brady and Acrivos.[13]

The second interesting point is that the solutions to the moderate injection and suction cases all tend to the same respective curve with increasing Reynolds numbers. As $|R|$ increases in the injection case, the relative importance of α diminishes; and ultimately, $|\alpha/R|$ becomes sufficiently small regardless of the expansion or contraction rate. For $|\alpha/R|<0.1$, the dimensionless velocity becomes indistinguishable from the inviscid Taylor profile given by $\sin(\frac{1}{2}\pi\eta)$.[7]

In the suction case, however, one needs to measure the effective suction Reynolds number, R_s. As R_s is successively increased above 20, the normal velocity becomes increasingly more linear. It approaches its expected value of $v^*=\eta$ for an inviscid suction flow.[2,6] For this reason, large injection or suction cases are not always shown whenever the corresponding curves are found to cluster very near the inviscid solution.

C. Normal and streamwise pressure distributions

Figure 5 exhibits the normal pressure drop of low and moderate values of the cross-flow Reynolds number for various expansion/contraction cases. For every level of injection or suction save one, the absolute pressure change is at its largest near the wall. The deviant to this trend is the scenario involving low suction with a rapidly expanding channel ($R=-1$ at $\alpha=10$). Referring back to the streamwise velocity profile for this particular case [shown Fig. 3(a)], one can observe that appreciable flow reversal accompanies this combination of operating parameters.

Moving on, one may also note that, in general, increasing the rate of wall contraction during injection increases the pressure drop. Additionally, increasing the expansion rate during suction also increases the pressure drop until flow reversal occurs. For an injection–expansion process, or a suction–contraction process, the pressure drop diminishes with the successive increases in $|\alpha|$.

The parabolic behavior of the streamwise pressure distribution is captured in Fig. 6. Here one may note that the higher the wall contraction rate, the greater the absolute pressure change. That is, the absolute pressure drop is reduced as $|\alpha|$ is diminished. Moreover, one also observes that the pressure drop is typically favorable (i.e., negative) for injection with contraction; however, when expansion becomes sufficiently large, flow reversal occurs and the pressure drop switches signs (see $R=20$ and $\alpha=100$). For a suction-driven process, the converse is true. In the case of a suction–contraction process, the pressure drop is favorable (positive for the suction flow). It may however turn to adverse (negative) when the expansion rate becomes sufficiently large (see $R=-20$ and $\alpha=10$). The adverse pressure drops are consistent with the criteria established above.

D. Wall shear stress distribution

Figure 7 illustrates the effects of varying the governing parameters on the character of the shear stress at the wall. For the same physical reasons, the trends accompanying the shear stress are identical to those associated with the streamwise pressure behavior. On that account, an injection–contraction process leads to a negative (favorable) shear stress that opposes the primary direction of motion. However, when expansion increases beyond a certain level, flow reversal occurs and the shear stress turns slightly positive (e.g., $R=20$ and $\alpha=100$). That condition is established when the flow injected moves to the head-end first, before turning downstream. For a suction–contraction process, the shear stress is positive (favorable) until expansion is sufficiently large. For example, when $R=-20$ and $\alpha=5,10$ in Fig. 7(b), the shear stress turns negative, owing to flow reversal. Since flow reversal occurs when the shear stress at the wall changes sign, the stress must pass through zero at some point such that $\tau=\partial u/\partial y|_w=0$. Thus, calculating the zeroes of the wall shear stress can enable us to determine the criterion for flow reversal. For the cases of suction in Fig. 6(b), we observe that the shear stress at the wall increases as the contraction ratio $|\alpha|$ is increased. This can be attributed to the increased skin friction associated with rapid wall motion in comparison to the stationary wall case. In the latter, the shear stress variation is typically small, but increases in the downstream direction. Notably, it becomes larger at higher suction rates due to thinning boundary layers and steeper slopes at the wall.

E. Streamlines

Streamlines originating or terminating at several discrete points along the length of the wall are presented in Fig. 8 over a wide range of cross-flow Reynolds numbers and expansion ratios. We can clearly see that injection tends to push

the streamlines closer to the core while suction draws them somewhat away from the core and closer to the wall. In the same vein, large suction promotes a more abrupt change in the flow direction from streamwise to normal. This tends to be accompanied by sharper flow turning near the wall. Conversely, cases with rapidly expanding walls will experience delayed flow turning and flow reversal—as hinted at earlier. These differences in streamline curvature, and hence, the flow turning rate, become more appreciable when we focus our attention further downstream. Thus, the effects of viscosity are more significant in the downstream portions of the channel. The same can be said of vorticity effects which, in our problem, are directly proportional to the shearing stress in view of $v=v(y)$.

In turning our attention to the effects of α, we observe that the higher the expansion speed, the longer the normal velocity will be large in comparison to its streamwise counterpart as $y\to 0$. One can then imagine a purely hypothetical scenario where the walls expand at nearly the same speed as that of the fluid entering the channel. Thus, when $\dot{a}=v_b$, the expansion process offsets the effect of injection to the point that streamlines will exhibit an infinite radius of curvature and remain perpendicular to the walls. If this situation occurs, the flow turning will be delayed indefinitely with the cessation of downstream motion.

VI. CONCLUSIONS

The current analysis presents a procedure that establishes an exact similarity solution of the Navier–Stokes equations in semi-infinite rectangular channels with porous and uniformly expanding walls. It is found that in rectangular chambers and ducts where wall regression and injection occur simultaneously, the streamlines, pressure distributions, and shear stresses are time and space dependent. They can be characterized by two dimensionless parameters: the expansion ratio of the walls α and the cross-flow Reynolds number R. A shooting method, coupled with a Runge–Kutta integration scheme, were utilized to numerically solve the fourth order differential equation. The results contributed to further explain the physics behind the flow field character. In summary, interesting structures were observed including the formation of regions where flow reverses near the head-end section of the channel. These regions are typically found when the relative expansion ratio is large, namely

$$|\alpha/R|\geqslant\begin{cases}10, & \text{injection}\\ 1, & \text{suction}\end{cases}. \tag{37}$$

On the other hand, for sufficiently large $|R|$, solutions are found to asymptote to the inviscid flow analogue in a porous channel for which Taylor's sinusoidal profile for injection,[7] or Sellars' linear profile for suction become suitable approximations.[6] In fact, results become hardly distinguishable when

$$|\alpha/R|<0.1, \tag{38}$$

for injection. For suction, the criterion must be based on the effective Reynolds number, $R_s=-(R+\alpha)$. Accordingly, the current solution will resemble Sellar's inviscid profile for $R_s>20$. These criteria extend our understanding of laminar flows in porous channels. Further studies addressing multiple asymptotic solutions and the onset and evolution of flow instability would complement this analysis and promote additional comprehension of flows in deformable channels with porous walls. In particular, experimental investigations of suction-driven channel flows would be desirable at this point to help confirm or refute current speculations.

APPENDIX: NUMERICAL STRATEGY

We begin by differentiating Eq. (24) with respect to η to obtain

$$F^{IV}+FF'''+F''(3\alpha-F')+\alpha\eta F'''=0, \tag{A1}$$

which can be solved numerically using a shooting method and fourth-order Runge–Kutta integration.

1. Transforming the boundary value ODE into initial value PDEs

We can express Eq. (A1) in the classic form

$$y^{IV}=f(x,y,y',y'',y''')=y''(y'-3\alpha)-yy'''-\alpha xy'''. \tag{A2}$$

Two new variables τ and κ are introduced as user-specified initial guesses at $x=0$ in the solution. Then, as permitted by the chain rule, the order of differentiation in Eq. (A2) can be switched such that

$$\frac{\partial}{\partial\tau}[f(x,y,y',y'',y''')]$$

$$=\frac{\partial(y_{xxxx})}{\partial\tau}=\frac{\partial}{\partial\tau}\left(\frac{\partial^4 y}{\partial x^4}\right)=\frac{\partial^4}{\partial x^4}\left(\frac{\partial y}{\partial\tau}\right). \tag{A3}$$

Two new functions T and K can now be posited via

$$\mathrm{T}(x,\tau,\kappa)\equiv\frac{\partial y}{\partial\tau}\ \text{ and }\ \mathrm{K}(x,\tau,\kappa)\equiv\frac{\partial y}{\partial\kappa}. \tag{A4}$$

Fourth-order differential equations for T and K can be derived from Eq. (A3) in the form

$$\frac{\partial^4}{\partial x^4}\left(\frac{\partial y}{\partial\tau}\right)=\mathrm{T}_{xxxx}=\frac{\partial f}{\partial x}\frac{\partial x}{\partial\tau}+\frac{\partial f}{\partial y}\frac{\partial y}{\partial\tau}+\frac{\partial f}{\partial y'}\frac{\partial y'}{\partial\tau}+\frac{\partial f}{\partial y''}\frac{\partial y''}{\partial\tau}+\frac{\partial f}{\partial y'''}\frac{\partial y'''}{\partial\tau},$$

$$\mathrm{T}_{xxxx}=f_y\mathrm{T}+f_{y'}\mathrm{T}_x+f_{y''}\mathrm{T}_{xx}+f_{y'''}\mathrm{T}_{xxx}, \tag{A5}$$

$$\mathrm{K}_{xxxx}=f_y\mathrm{K}+f_{y'}\mathrm{K}_x+f_{y''}\mathrm{K}_{xx}+f_{y'''}\mathrm{K}_{xxx}.$$

The BCs from Eq. (A1) can be written using τ and κ as follows:

$$y(0)=0,\quad y'(0)=\tau,\quad y''(0)=0,\quad y'''(0)=\kappa. \tag{A6}$$

Two remaining relations are required to satisfy the endpoint BCs at $\eta=1$ ($x=1$ in the current transformation). This is accomplished by introducing the functions $g(\tau,\kappa)$ and $h(\tau,\kappa)$ such that

$$g(\tau,\kappa)=y(1,\tau,\kappa)-R=0,\quad h(\tau,\kappa)=y'(1,\tau,\kappa)-0=0. \tag{A7}$$

Based on Newton's generalized method, an algorithm for calculating the zeros τ^* and κ^* of Eq. (A7) can be implemented. The algorithm requires updating the initial guesses via

$$\begin{bmatrix}\tau\\ \kappa\end{bmatrix}_{n+1}=\begin{bmatrix}\tau\\ \kappa\end{bmatrix}_{n}-[J]^{-1}\cdot\begin{bmatrix}y(1,\tau,\kappa)-R\\ y'(1,\tau,\kappa)\end{bmatrix}_{n}, \tag{A8}$$

where n is the iteration index and $[J]^{-1}$ is the inverted Jacobian matrix. The Jacobian is defined as

$$J=\begin{bmatrix}\partial f_1/\partial\tau & \partial f_1/\partial\kappa\\ \partial f_2/\partial\tau & \partial f_2/\partial\kappa\end{bmatrix}=\begin{bmatrix}\mathrm{T}(1) & \mathrm{K}(1)\\ \mathrm{T}_x(1) & \mathrm{K}_x(1)\end{bmatrix}\quad\begin{matrix}f_1=y-R\\ f_2=y'\end{matrix}. \tag{A9}$$

Once $[J]^{-1}$ is determined, Eq. (A8) reduces to

$$\begin{bmatrix}\tau\\ \kappa\end{bmatrix}_{n+1}=\begin{bmatrix}\tau\\ \kappa\end{bmatrix}_{n}-c\begin{bmatrix}\mathrm{K}_x(1) & -\mathrm{K}(1)\\ -\mathrm{T}_x(1) & \mathrm{T}(1)\end{bmatrix}\begin{bmatrix}y-R\\ y'\end{bmatrix}_{n}, \tag{A10}$$

where $c=1/\det(J)$. Following the transformation from Eq. (A4), the BCs can then be derived to yield

$$\begin{aligned}&\mathrm{T}(0,\tau,\kappa)=0,\quad \mathrm{T}_{xx}(0,\tau,\kappa)=0,\\ &\mathrm{K}(0,\tau,\kappa)=0,\quad \mathrm{K}_{xx}(0,\tau,\kappa)=0,\\ &\mathrm{T}_x(0,\tau,\kappa)=1,\quad \mathrm{T}_{xxx}(0,\tau,\kappa)=0,\\ &\mathrm{K}_x(0,\tau,\kappa)=0,\quad \mathrm{K}_{xxx}(0,\tau,\kappa)=1.\end{aligned} \tag{A11}$$

Our diligence in the above exercise enabled us to transform the fourth-order ODE of Eq. (A1) and its BCs into the three coupled ODEs of Eqs. (A2) and (A5).

2. Runge–Kutta steps

The shooting method described above can now be easily converted into a ready-to-integrate Runge–Kutta solution set. We begin by assigning 12 variables to represent y, T, K, and their respective derivatives out to the third-order: $\boldsymbol{Y}=[y_j]=[y\ \mathrm{T}\ \mathrm{K}\ y'\ \mathrm{T}_x\ \mathrm{K}_x\ y''\ \mathrm{T}_{xx}\ \mathrm{K}_{xx}\ y'''\ \mathrm{T}_{xxx}\ \mathrm{K}_{xxx}]^{\mathrm{T}}$. Through similar substitution, the associated initial conditions can also be evaluated, thereby providing $\boldsymbol{Y}(0)=[y_j(0)]=[0\ 0\ 0\ \tau\ 1\ 0\ 0\ 0\ 0\ \kappa\ 0\ 1]^{\mathrm{T}}$. Finally, the solution requires the input of initial guesses for τ and κ which are then updated according to

$$\begin{aligned}\tau_{n+1}&=\tau_n+\frac{\mathrm{K}(1)y'(1)+\mathrm{K}_x(1)[R-y(1)]}{\mathrm{T}(1)\mathrm{K}_x(1)-\mathrm{K}(1)\mathrm{T}_x(1)},\\ \kappa_{n+1}&=\kappa_n+\frac{\mathrm{T}_x(1)[y(1)-R]-\mathrm{T}(1)y'(1)}{\mathrm{T}(1)\mathrm{K}_x(1)-\mathrm{K}(1)\mathrm{T}_x(1)}.\end{aligned} \tag{A12}$$

[1] A. S. Berman, "Laminar flow in channels with porous walls," J. Appl. Phys. **24**, 1232 (1953).
[2] R. M. Terrill, "Laminar flow in a uniformly porous channel," Aeronaut. Q. **15**, 299 (1964).
[3] I. Proudman, "An example of steady laminar flow at large Reynolds number," J. Fluid Mech. **9**, 593 (1960).
[4] M. Morduchow, "On laminar flow through a channel or tube with injection: Application of method of averages," Q. J. Appl. Math. **14**, 361 (1957).
[5] F. M. White, Jr., B. F. Barfield, and M. J. Goglia, "Laminar flow in a uniformly porous channel," Trans. ASME, J. Appl. Mech. **25**, 613 (1958).
[6] J. R. Sellars, "Laminar flow in channels with porous walls at high suction Reynolds numbers," J. Appl. Phys. **26**, 489 (1955).
[7] G. I. Taylor, "Fluid flow in regions bounded by porous surfaces," Proc. R. Soc. London **234**, 456 (1956).
[8] S. W. Yuan, "Further investigation of laminar flow in channels with porous walls," J. Appl. Phys. **27**, 267 (1956).
[9] R. M. Terrill, "Laminar flow in a uniformly porous channel with large injection," Aeronaut. Q. **16**, 323 (1965).
[10] R. M. Terrill and G. M. Shrestha, "Laminar flow through parallel and uniformly porous walls of different permeability," J. Appl. Math. Phys. **16**, 470 (1965).
[11] G. M. Shrestha and R. M. Terrill, "Laminar flow with large injection through parallel and uniformly porous walls of different permeability," Q. J. Mech. Appl. Math. **21**, 413 (1968).
[12] S. M. Cox, "Two-dimensional flow of a viscous fluid in a channel with porous walls," J. Fluid Mech. **227**, 1 (1991).
[13] J. F. Brady and A. Acrivos, "Steady flow in a channel or tube with an accelerating surface velocity. An exact solution to the Navier–Stokes equations with reverse flow," J. Fluid Mech. **112**, 127 (1981).
[14] E. B. B. Watson, W. H. H. Banks, M. B. Zaturska, and P. G. Drazin, "On transition to chaos in two-dimensional channel flow symmetrically driven by accelerating walls," J. Fluid Mech. **212**, 451 (1990).
[15] P. Watson, W. H. H. Banks, M. B. Zaturska, and P. G. Drazin, "Laminar channel flow driven by accelerating walls," Eur. J. Appl. Math. **2**, 359 (1991).
[16] W. H. H. Banks and M. B. Zaturska, "On flow through a porous annular pipe," Phys. Fluids A **4**, 1131 (1992).
[17] L. Durlofsky and J. F. Brady, "The spatial stability of a class of similarity solutions," Phys. Fluids **27**, 1068 (1984).
[18] S. W. Yuan and E. W. Brogren, "Turbulent flow in a circular pipe with porous walls," Phys. Fluids **4**, 368 (1961).
[19] G. Casalis, G. Avalon, and J.-P. Pineau, "Spatial instability of planar channel flow with fluid injection through porous walls," Phys. Fluids **10**, 2558 (1998).
[20] J. Griffond and G. Casalis, "On the dependence on the formulation of some nonparallel stability approaches applied to the Taylor flow," Phys. Fluids **12**, 466 (2000).
[21] J. Griffond and G. Casalis, "On the nonparallel stability of the injection induced two-dimensional Taylor flow," Phys. Fluids **13**, 1635 (2001).
[22] J. Barron, J. Majdalani, and W. K. Van Moorhem, "A novel investigation of the oscillatory field over a transpiring surface," J. Sound Vib. **235**, 281 (2000).
[23] J. Majdalani, J. Barron, and W. K. Van Moorhem, "Experimental classification of turbulence in an oscillatory channel flow with transpiring walls," ASME FEDSM 2001-1881, New Orleans, LA, 2001.
[24] Y. Ma, W. K. Van Moorhem, and R. W. Shorthill, "Experimental investigation of velocity coupling in combustion instability," J. Propul. Power **7**, 692 (1991).
[25] Y. Ma, W. K. Van Moorhem, and R. W. Shorthill, "Innovative method of investigating the role of turbulence in the velocity coupling phenomenon," ASME J. Vibr. Acoust. **112**, 550 (1990).
[26] W. E. Wageman and F. A. Guevara, "Fluid flow through a porous channel," Phys. Fluids **3**, 878 (1960).
[27] V. N. Varapaev and V. I. Yagodkin, "Flow stability in a channel with porous walls," Fluid Dyn. **4**, 91 (1969).
[28] G. D. Raithby and D. C. Knudsen, "Hydrodynamic development in a duct with suction and blowing," Trans. ASME, J. Appl. Mech. **41**, 896 (1974).
[29] A. A. Sviridenkov and V. I. Yagodkin, "Flow in the initial sections of channels with permeable walls," Fluid Dyn. **11**, 689 (1976).
[30] M. Goto and S. Uchida, "Unsteady flows in a semi-infinite expanding pipe with injection through wall," Trans. Japan Soc. Aeronaut. Space Sci. **33**, 14 (1990).
[31] S. Uchida and H. Aoki, "Unsteady flows in a semi-infinite contracting or expanding pipe," J. Fluid Mech. **82**, 371 (1977).
[32] K. Hiemenz, "Die Grenzschricht an einem in den gleichförmigen Flüssigkeitsstrom eingetauchten geraden Kreiszylinder," Dingler's Polytech. J. **326**, 344 (1911).
[33] R. M. Terrill, "Laminar flow through a porous tube," ASME J. Fluids Eng. **105**, 303 (1983).
[34] M. B. Zaturska, P. G. Drazin, and W. H. H. Banks, "On the flow of a viscous fluid driven along a channel by suction at porous walls," Fluid Dyn. Res. **4**, 151 (1988).
[35] M. B. Zaturska and W. H. H. Banks, "Suction-driven flow in a porous pipe," J. Appl. Math. Mech. (ZAMM) **75**, 21 (1995).
[36] S. M. Cox and A. C. King, "On the asymptotic solution of a high-order

nonlinear ordinary differential equation,'' Proc. R. Soc. London **453**, 711 (1997).
[37]J. R. King and S. M. Cox, ''Asymptotic analysis of the steady-state and time-dependent Berman problem,'' J. Eng. Math. **39**, 87 (2001).
[38]W. A. Robinson, ''The existence of multiple solutions for the laminar flow in a uniformly porous channel with suction at both walls,'' J. Eng. Math. **10**, 23 (1976).
[39]K.-G. Shih, ''On the existence of solutions of an equation arising in the theory of laminar flow in a uniformly porous channel with injection,'' SIAM (Soc. Ind. Appl. Math.) J. Appl. Math. **47**, 526 (1987).
[40]C. Lu, ''On the asymptotic solution of laminar channel flow with large suction,'' SIAM (Soc. Ind. Appl. Math.) J. Math. Anal. **28**, 1113 (1997).
[41]C. Lu, ''On the asymptotic behavior of laminar flow through a porous pipe,'' Proceedings of the First World Congress of Nonlinear Analysis, Tampa, FL, 1996.
[42]C. Lu, ''On the existence of multiple solutions of a boundary value problem arising from laminar flow through a porous pipe,'' Can. Quart. Appl. Math. **2**, 361 (1994).
[43]J. F. Brady, ''Flow development in a porous channel or tube,'' Phys. Fluids **27**, 1061 (1984).